Automated Damage and Defect Detection with Low-Cost X-Ray Radiography using Data-driven Predictor Models and Data Augmentation by X-Ray Simulation

Stefan Bosse

[1]University of Bremen, Dept. Mathematics & Computer Science, Bremen

Abstract — **Detection of hidden defects in materials using X-ray images is still a challenge. Often a lot of defects are not directly visible in visual inspection. In this work, a data-driven feature marking model is introduced performing semantic pixel annotation. Input data is delivered by a standard industrial X-ray instrument (named MidQ, reference device) and a low-cost self-constructed portable X-ray instrument (named LowQ), which is introduced in detail in this work, too. Technical details of the X-ray instrument are relevant since the quality of the feature detector is compared with respect to noise, contrast, and signal quality of the MidQ and LowQ devices. Finally, simulation of X-ray images is used to provide a ground truth data set for the training of the feature detector. It can be shown that this approach is suitable to detect hidden pores in high-pressure die casted aluminum plates.**

Keywords — *Non-destructive Testing, Damage Diagnostics, X-ray Radiography, Computer Tomography, Feature Detection, Machine Learning*

1. Introduction

It is still difficult to identify and detect hidden faults or impurities in multi-layered composites like fiber-metal laminates (FML) as well as in homogeneous materials, e.g., high-pressure die casted aluminum materials, even using advanced X-ray Computer Tomography (CT). For example, an impact damage can be nearly invisible by a frontal X-ray projection, although, the deformation can be seen and detected manually by hand perception. Hidden pores in materials can be detected and analyzed by 3D CT volume rendering, but hard to be identified in single projection images (Radiography). Things are getting more worse if a portable low-cost X-ray radiography or semi-tomography machine is used (called Low-Q measuring device), as introduced and described in this work.

It is desirable to detect or mark defects, damages, or impurities by an automated feature marking system directly in the measure images. The impact of image quality can be relevant to the feature detection quality, regardless of the complexity of the model behind [1]. Often complex Neural Networks (Deep models) are used [2]. In this work, a simple pixel classifier is used. Semantic pixel detectors are simple mathematical models that can be used to mark Region of Interests (ROI) in an image relating to a specific semantic class. After the image preprocessing and filtering stages, damage and material faults are identified by a pixel anomaly detector, basically an advanced Convolutional Neural Network (CNN) and region-proposal R-CNN models. Training of pixel classifiers can use a few images only because each pixel region is a sample instance. R-CNN models require an extended sample data base, which cannot be acquired only by physical measurements. The training and test data set will always limited by a limited number of specimens, e.g., with impact damages, and a limited variance in material and damage parameters (e.g., location). For this reason, the data set is extended by synthetic data augmentation using X-ray simulation. In contrast to other wave measurement principles like Guided Ultrasonic Waves (GUW), X-ray images can be simulated with high ac-

curacy (compared with physically measured images). We are using the gVirtualXray software library [3,4] performing X-ray image simulation by using GPU processing only and ray-tracing. GvirtualXray is proven for its suitability to produce accurate images as long as diffraction and reflection of X-rays are neglected. In addition, a novel few projection hidden-damage detection methodology is introduced that can be used in-field with a portable X-ray machine as described above. Preliminary results show a high defect detection rate for a wide range of materials.
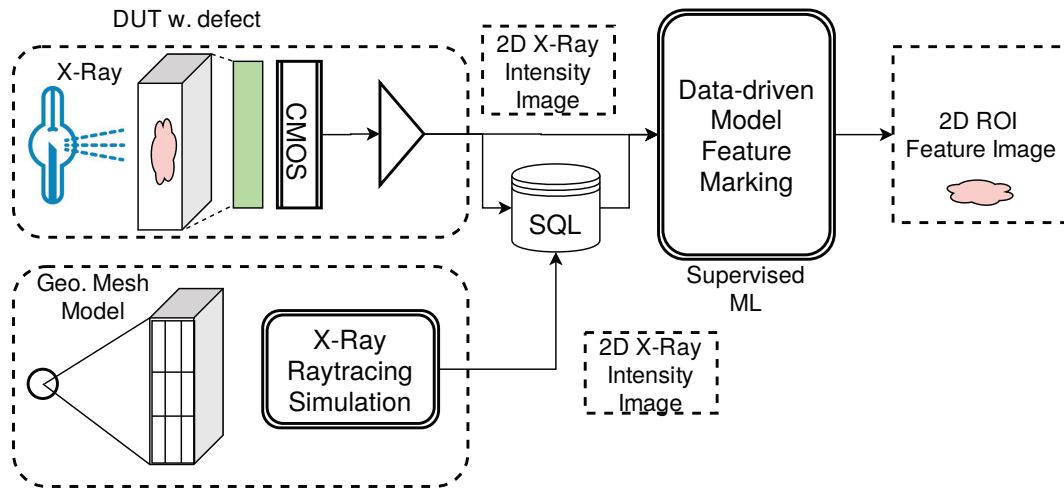

Fig. 1. The basic framework combining experimental measuring data with simulated data

A X-ray measuring system consists of a X-ray source (commonly cone beam with a specific focal size diameter *fsd*) and a X-ray detector. The X-ray source uses either a cold-emission or hot-emission (Coolidge) X-ray tube. In cold-emission, the electrical field extracts and accelerates electrons from the cathode to the anode, in hot-emission there is a heated free electron source, and the electrical field only accelerates the electron to a target anode material. Cold emission tubes lack independent tube current control (dependent on the tube voltage).

The X-ray detector can be a direct or indirect conversion system. In a direct conversion system the X-ray photons will generate electrons (photo effect) directly in the solid-state device, in an indirect conversion system a conversion material (scintillator) is required to convert X-ray photons into visible light photons, finally converted to electrons in a solid-state detector.

In addition to the X-ray conversion mode, there are direct coupled detectors and imaging systems that map the X-ray converted image from a scintillator onto a solid-state detector. Direct coupled systems require an optical coupling material, commonly a fiber optics plate (FOP) posing high geometric accuracy and low distortion. An indirect imaging system with a lens-based imaging system introduces optical distortion with reduced geometric accuracy, but having the advantage of low costs [5].

Solid-state detectors are typically Coupled Charge Devices (CCD) or CMOS pixel detectors. Although, used in an indirect conversion system sensitive to visible light, the are still sensitive to incident X-ray radiation producing shot or popcorn noise.

The X-ray equipment consists of a low-cost X-ray source for dental diagnostics and an X-ray detector consisting of a conventional medical X-ray converter and amplifier foil (Fine 100) backside imaged by a commercially available CMOS monochrome image sensor (back-illuminated Sony IMX290 2M pixel sensor) and a simple two-lens optics. The optical distortion introduced by the optics increases with increasing distance

from the center of the image ("barrel distortion") and must be corrected, at least for CT 3D volume reconstruction.

The measured X-ray images pose increased spatially equally distributed non-gaussian noise (compared with high-quality flat panel detectors) and more important randomly located "popcorn" shot noise by avalanche effects in pixels and pixel clusters (islands) due to X-ray radiation exposure (back-illuminated sensors are very sensitive for this noise). The gaussian noise can be reduced by averaging, the shot noise is removed by using multiple images recorded in series and an automated pixel replacement algorithm. The shot noise is a seed threshold phenomena, i.e., the location and number of white pixels changes from image to image, therefore allowing the replacement of white pixels in one image from unaltered pixels from another image.

Basically we can classify X-ray measuring devices and systems into three classes with respect to Non-destructive Testing (NDT) in engineering, especially for metals and composite materials:

1. HighQ: Micro CT devices with micro focus tubes with optional optical magnification (focal spot diameter below 50 μm), effective resolution below 100microm, SNR > 200;

2. MidQ: Industrial systems (standard focal spot diameter above 200 μm, typically 0.8 mm), effective resolution above 100microm, SNR > 100;

3. LowQ: Low-cost system (standard focal spot diameter above 500 μm, typically 0.8 mm), effective resolution typically above 50microm, SNR < 100.

The classification quality relies on resolution, contrast, and noise. In the following section we only distinguish between a low-cost and self-constructed LowQ and an industrial MidQ instrument as a reference with standard focal spot diameters of about 0.8 mm. The low-cost X-ray measuring instrument (< 1000€) should be an alternative for laboratory and industrial devices that are much more expensive (> 100000€). The technical and construction details are important to compare the device classes.

2. X-ray Radiography and CT Systems

Two experimental setups are used in this work delivering input data for the training and test of the automated damage feature marking model:

1. MidQ: Laboratory Radiography and CT system (Fraunhofer IFAM), electron beam focus spot diameter 0.75 mm (Wolfram anode material), anode voltage 50-120 kV, tube current up to 10 mA, direct imaging solid-state detector 1000 × 1000 pixels, detector pixel size 200μm

2. LowQ: Self-constructed mobile low-cost Radiography and CT system, electron beam focus spot diameter 0.8 mm (Wolfram anode material), anode voltage 30-70 kV, tube current up to 1 mA, indirect imaged monochrome and back illuminated CMOS camera sensor (1920 × 1080 pixels), detector pixel size 3μm, image-scaled virtual detector pixel size 35μm, X-ray scintillator screen (Ortho Fine 100 foil).

2.1 Low-Cost X-Ray Device

The first device is only a reference system used to derive material and structure models and to compare with the low-cost system introduced in this work. The architecture and the main components of the proposed low-cost LowQ X-ray measuring device is shown in Fig. 2. A low-cost commercial wolfram X-ray tube with a focal spot diameter of 0.8 mm and a typical anode voltage range of 30-80kV is used. The imaging system consists of a widely used X-ray intensifier screen (Ortho Fine 100) and a commercial CMOS camera with a double lens optics. The entire X-ray measuring device is controlled by an embedded computer (Raspberry Pi 4). The camera and the device controls can be accessed via a Web browser remotely.

The X-ray tube is a KL 27-0.8-70 based on a classical Coolidge principle (hot emission tube). The focal spot diameter is about 0.8 mm with a opening angle of 19° (i.e., 70 mm spot diameter at 200 mm distance). The X-ray beam current can be controlled by the heater independently from the X-ray anode voltage (maximal tube current is 10 mA). Nearly most of the electrical input power is converted into heat in the tube

anode. Even low tube currents about 1 mA produces a heat power of more than 50 W, raising the temperature of the anode far beyond 100 °C (measured with a thermographhy camera). The heat must be propagated outside the tube, here by an attached massive Cooper cylinder (see right side of the tube in Fig. 3, detail view of the X-ray source) and a ventilator. With this cooling, the anode temperature can be kept below 40°C for operating times below one Minute.

The camera consists of a commercial monochrome CMOS back-illuminated image sensor (Sony IMX 290) providing 1920x1080 pixels with 3μm × 3μm pixel size. The CMOS sensor supports high exposure times (5 s and longer) by posing low-noise output. The optical imaging system consists of a zoomable double lens system mapping the backside of the scintillator screen on the image sensor. With the given distance of 125 mm (see Fig. 2 (b)) between screen and image sensor, the effective Field of View (FOV) is about 65 × 36 mm (effective image size is 30 μm).

The X-ray source unit, the X-ray detector unit, and the optional rotation stage are controlled by an embedded computer (Raspberry Pi 4), which is connected to a LAN. The instrument can be accessed via a Web browser. There is one main application program running on the embedded computer. The program controls the camera (using a vendor SDK, ToupTek photonics) and captures images via USB, the X-ray unit and rotation stage stepper motor via a GPIO port. A Geiger counter is used to monitor the X-ray intensity. The remote access is provided via a HTTP service, providing the HTML control page, too (embedded in the software).
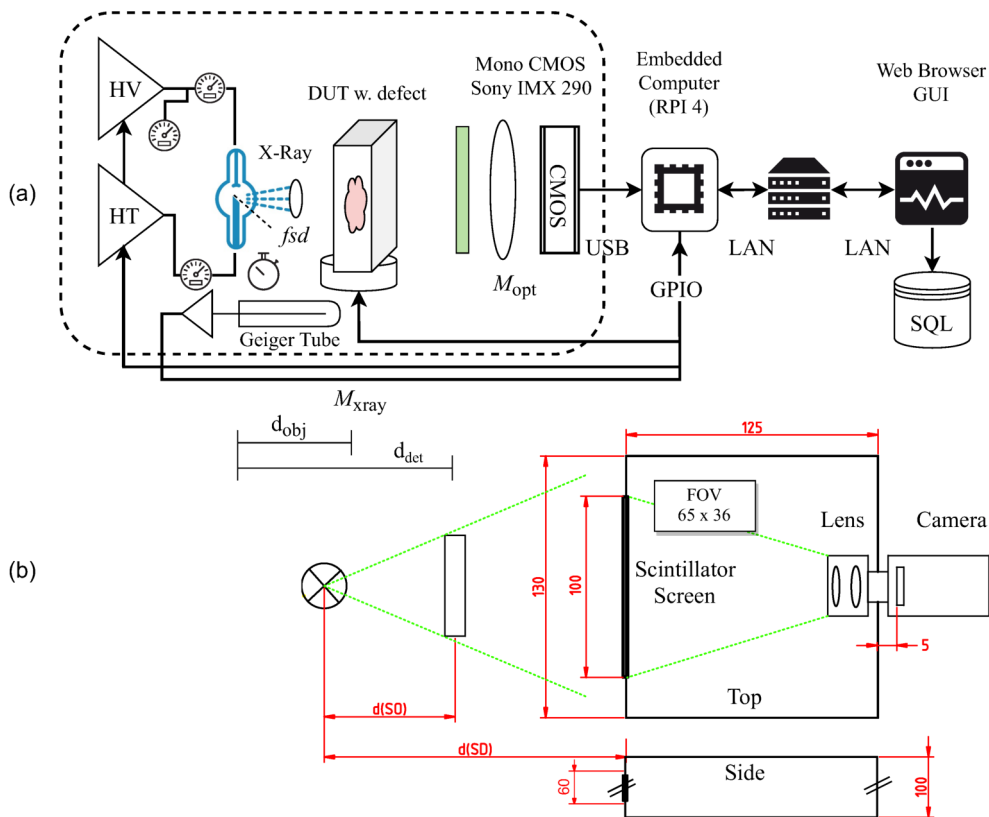

Fig. 2. Low-cost X-ray Radiography and CT instrument (a) General overview (b) Details of the detector (all dimensions in mm)
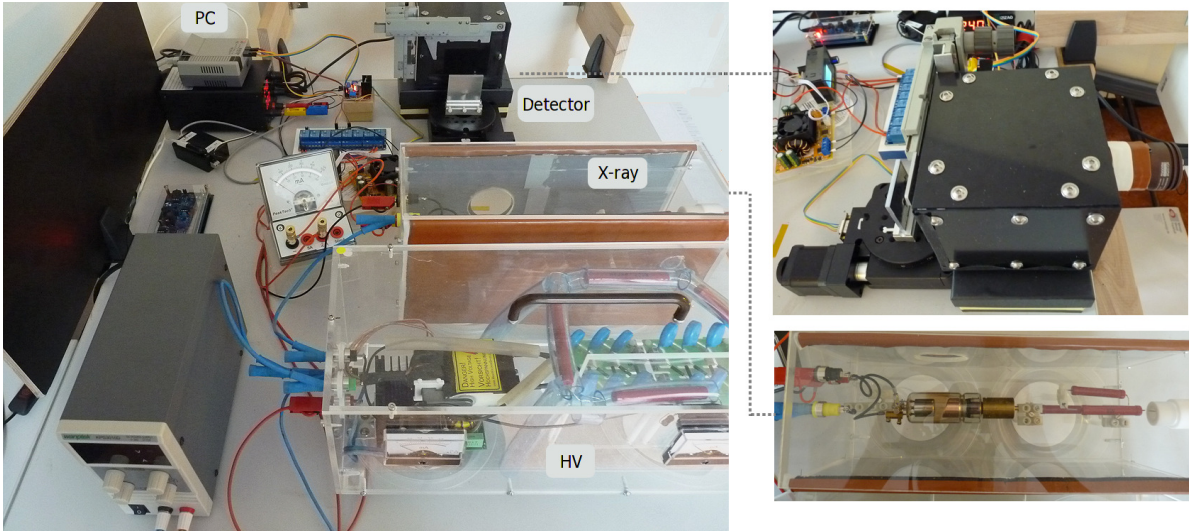
Fig. 3. Prototype of the low-cost X-ray Radiography and CT instrument
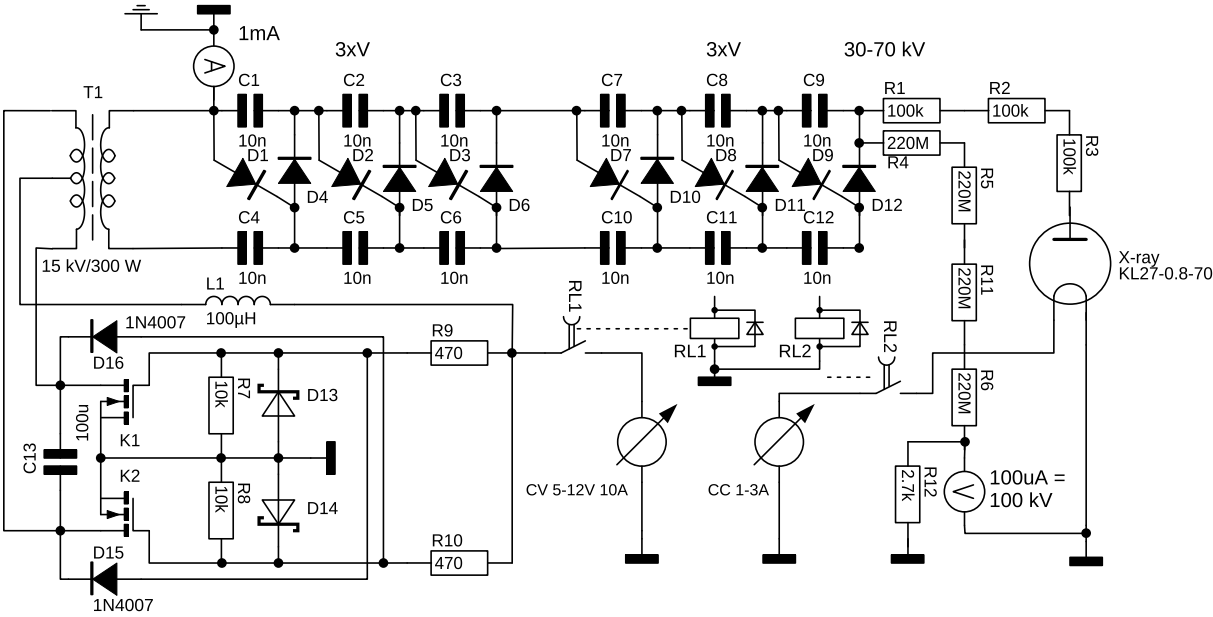

Fig. 4. Electronic schematic of the low-cost X-ray source

2.2 Electronics

The electronic schematic of the X-ray source is shown in Fig. 4. The circuit consists of a high-voltage generator, a electron heater constant current supply, and relay switches connected to the embedded computer. The high-voltage generator uses a classical discrete zero voltage switching (ZVS) driver circuit to drive a high-voltage transformer. The input voltage of the ZVS determines the output voltage of transformer $T1$ (about 40 kHz, input range 5-12 V, output voltage 5-12 kV). The output voltage of the high-voltage transformer is multiplied by a six-stage Villard cascade. The HV supply delivers up to 70 kV and 1 mA current (70 W). Neither the voltage nor the tube current is regulated by a feed-back loop, in contrast to industrial devices.

2.3 Detector

The resolution of a X-ray imaging system is limited mainly by two parameters:

1. Detector pixel size d_p multiplied by the optical image magnification, i.e., $d_p M_{opt}$;

2. The X-ray magnification M_{xray}.

The X-ray magnification is given by:

$$M_{xray} = \frac{d_{\text{det},src}}{d_{obj,src}}$$
$$a = (M_{xray} - 1)f_b \tag{1}$$

with f_b as the focal spot diameter (FSD), resulting in an imaging focus limit of about a (aperture limit) [6]. This formula shows that a magnification M_{xray} not necessarily increases the resolution. The aperture (blur) limit a increase with increasing magnification. For example, if we assume a detector pixel size of 200µm, a FSD of 0.8 mm, and a magnification of M=2, the resulting aperture limited resolution is about 0.8 mm!

The exposure time t_x defines the noise level and the source.to-noise ratio achievable with the given X-ray power P_x. The industrial reference MidQ system has a pixel area size of about 40 kµm^2, whereas the LowQ detector has a pixel area of only 9µm^2! The direct imaging MidQ system has a tight coupling of the scintillator to the detector pixels via a FOP, whereas the indirect imaging system poses optical losses in lenses and coupling components. The MidQ system requires typically exposure times in the order of 100 ms (with P_x=200 W), whereas the LowQ device requires at least 5000 ms (with P_x=50 W).

The camera deployed in the LoWQ device is a USB 2.0 Omegon Guide 2000 M Mono with a back-illuminated monochrome Sony IMX290 sensor. The optical imaging system consists of a CS-Mount double lens system with 2.8-12 mm focal length and f/1.4 aperture. The IMX290 image sensor uses an integrated 12 Bits ADC (directly accessible by a camera raw format) for image digitalization, compared with an external 16 Bits ADC used in the industrial MidQ detector.

The scintillator used in the detector has a normalized conversion factor 100 providing sufficient amplification and high resolution. The scintillator consists of phosphor materials based upon a mix of rare earths with a high luminous intensity and low graininess. The screen emission matches ideally the spectral sensitivity of the image sensor, as shown in Fig. 5 (relative sensitivity of 0.95 at main emission peak). A limiting resolution up to 10 Line Pairs (LP) / mm with 10 % contrast can be achieved. The contrast of the entire low-cost X-ray detector is about 70% at 2 LP/mm and about 25% at 8 LP/mm.
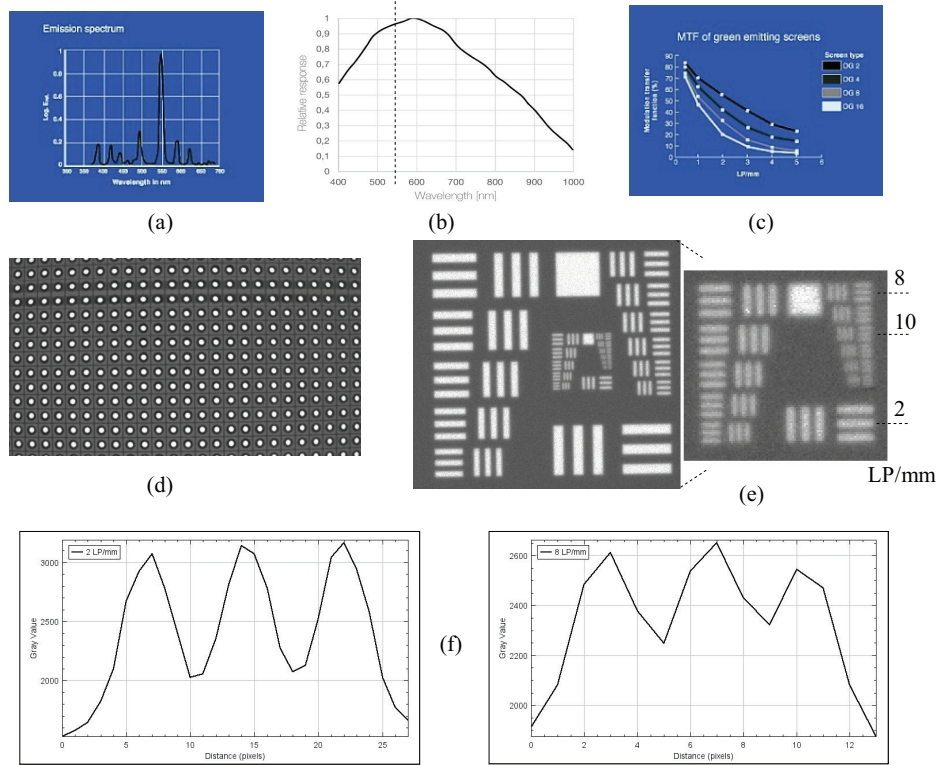
Fig. 5. (a) Emission spectrum of the scintillator material [7] (b) Spectral sensitivity of the IMX290 image sensor [8] (c) Resolution of the scintillator screen in dependence of the material thickness and amplification factor [7] (OG-2: conversion factor 100, OG-4: 200, and so on) (d) Dot pattern measured with LowQ X-ray detector (e) USAF 1951 pattern recorded with 55 kV/0.7 mA/average of 4 images (f) Intensity profiles and contrast at 2 an 8 LP/mm from (e)

2.4 Noise

The CMOS image sensor is sensitive to X-ray radiation, not too much to use the image sensor directly, but with respect to popcorn and shot noise. Popcorn noise is a random seed phenomenon, i.e., in some pixels there is an electron wall breakthrough leading to saturated (white) pixels. Fortunately, after the pixels are cleared (before the sampling of the next image), the saturation is eliminated and two succeeding images will commonly not pose the same flooded pixels.

Commonly, the image device is not directly exposed the X-ray beam. Instead, a mirror under an angle of 45° is used and the camera is placed with a 90° angle with respect to the X-ray beam axis (see [5], for example). We tried the same approach, but we observed:

1. An expected reduction of light intensity (mirror reflectivity < 1) and more geometric distortions;

2. There is still shot noise (although, strongly reduced, but not totally vanished).

The second observation is a result of the mirror construction. The mirror was a conventional industrial aluminum mirror mounted on an aluminum carrier under the same angle as the mirror. This combination still scatters some X-rays.

Therefore, we placed the camera again in the X-ray beam and using a simple multi-image noise compensation method. It removes shot noise, and reduces non-gaussian X-ray and gaussian (electronics) noise, too,
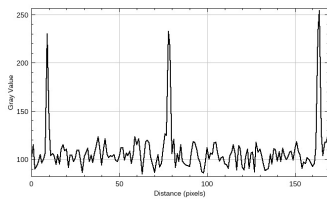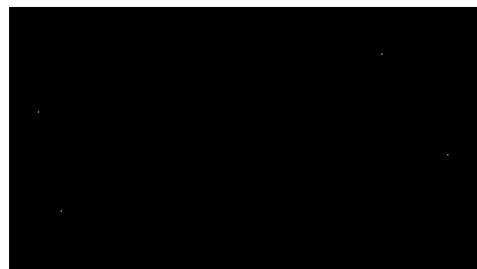
shown in Alg. 1. Examples and results are shown in Fig. 6. Choosing the γ threshold is crucial because not all shot noise pixels reach the maximum camera intensity, and some will only be reduced by averaging if they are below the chosen threshold.

Alg. 1. Shot (popcorn) noise removal and image averaging. γ is a noise threshold with respect to the image pixel value range (commonly $0.9max$) and Σ is a set of images. The result of the averaged and noise corrected image is σ_0
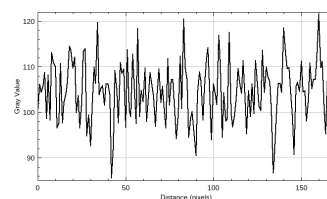

```
 1:  σ₀ := Σ[1]
 2:  ∀ (x,y) ∈ coord(σ₀) do
 3:    if σ₀[x,y] > γ then
 4:      ∀ σ in { Σ / σ₀ } do
 5:        if σ[x,y] < γ then
 6:          σ₀[x,y] := σ[x,y]
 7:          break
 8:        endif
 9:      done
10:    endif
11:    ∀ σ ∈ { Σ / σ₀ } do
12:      if σ[x,y] < γ then
13:        σ₀[x,y] := σ₀[x,y] + σ[x,y]
14:      else
15:        σ₀[x,y] := σ₀[x,y] + σ₀[x,y]
16:      endif
17:    done
18:    σ₀[x,y] := σ₀[x,y] / |Σ|
19:  done
```

(a) Without Noise Cancellation

(b) With Noise Cancellation (2 Im.)

Fig. 6. (Top) Example images without (left) and with (right) noise cancellation (Bottom) Example line intensity plots with flooded pixels (left) and residual noise only (right)

In addition to the shot noise there is gaussian electronics and detector noise (not correlated among pixels) and non-gaussian X-ray radiation and source noise, which can pose spatial correlation. In Sec. 5 and Fig. 10 the gaussian noise of images sampled by the LowQ and MidQ instruments are compared. The industrial MidQ device (including the X-ray source) has an average noise level SNR = $\overline{x}/\sigma$ = 280 (2σ noise interval is about 0.7%), whereas the LowQ device has an SNR = 95 (2σ noise interval is about 2%).

3. Simulation

As common in engineering applications, the data variance of experiments and specimens is limited. On one side, specimens with impacts damages pose a wide range of different micro and macro damages, e.g., delaminations, cracks, kissing bond defects, and many more. Therefore, the measurement (X-ray image) of one specimen delivers only a few features, and the number of specimens is limited, too. High-pressure Die casted aluminum specimens, on the other side, contain a high number of gas pores (here named defects), and the number of specimens can be high. Even if the feature and data variance is sufficient, there is no ground truth of the data, especially required for accurate labelling of training data for supervised Machine Learning (ML). For this reason, in this work X-ray images are computed (simulated) numerically from synthetic specimens based on a CAD model and Monte-Carlo simulation techniques, as shown in Fig. 7. The model is composed of Constructive Solid Geometry operations creating solid materials or defects (pores) by union or difference operations. The OpenSCAD software is used to convert the CSG model into a triangular mesh grid model (STL). This mesh model is finally processed by our own X-ray simulation software *XraySim*, based on the *gvxr/gVirtualXray* C++ software library [3] for computation of X-ray images.

The Monte Carlos simulation of the synthetic pores bases on a simple geometric ellipsoid model with a base parameter set derived from real pore analysis using CT reconstruction and projections measured with the MidQ device.
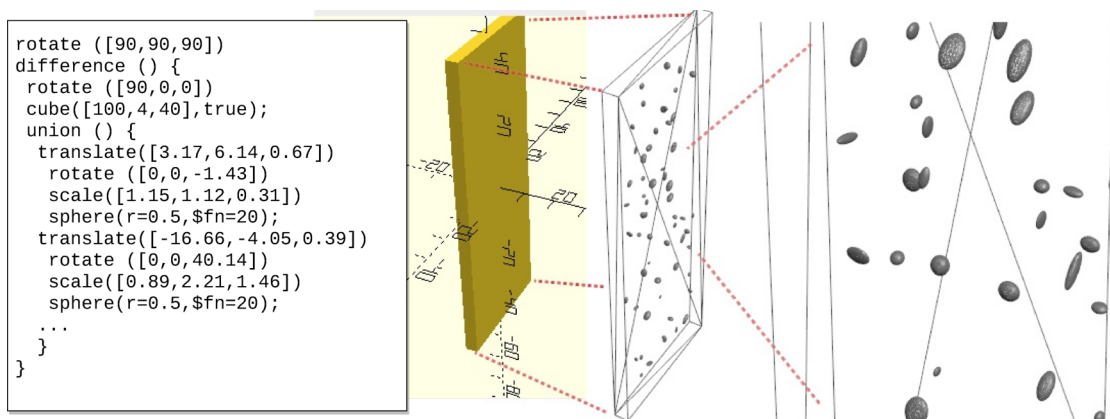


```
rotate ([90,90,90])
difference () {
 rotate ([90,0,0])
 cube([100,4,40],true);
 union () {
  translate([3.17,6.14,0.67])
   rotate ([0,0,-1.43])
   scale([1.15,1.12,0.31])
   sphere(r=0.5,$fn=20);
  translate([-16.66,-4.05,0.39])
   rotate ([0,0,40.14])
   scale([0.89,2.21,1.46])
   sphere(r=0.5,$fn=20);
  ...
 }
}
```

Fig. 7. Modelling of a die casted aluminum plate with gas pores using Monte Carlo simulation. Geometric parameters of real measure pores are used to create synthetic pores at random positions. (Left) Programmatic CSG model (Right) Rendered 3D model with synthetic pores (holes)

4. Feature Detector using a Semantic Pixel Classifier

The main objective of this work is to use an automated feature detector applied to single projection X-ray images delivered by a LowQ (low-cost) X-ray instrument to detect hidden defects in materials, here specifically pores in high-pressure die casted aluminum plates.

The input is a X-ray image, the output a feature map image that marks pores and provides there geometric parameters and position, as shown in Fig. 8. A pixel classifier is commonly implemented with a Convolutional Neural Network (CNN), mostly with only one or two convolution-pooling layer pairs. The input of the CNN is a sub-window masked out from the input image at a specific center position (x, y). The output is a class (or a real value in the range [0,1] as an indicator level for a class). The neighbouring pixels determine the classification result. th window with the CNN application is moved over the entire input image producing the respective feature output image.
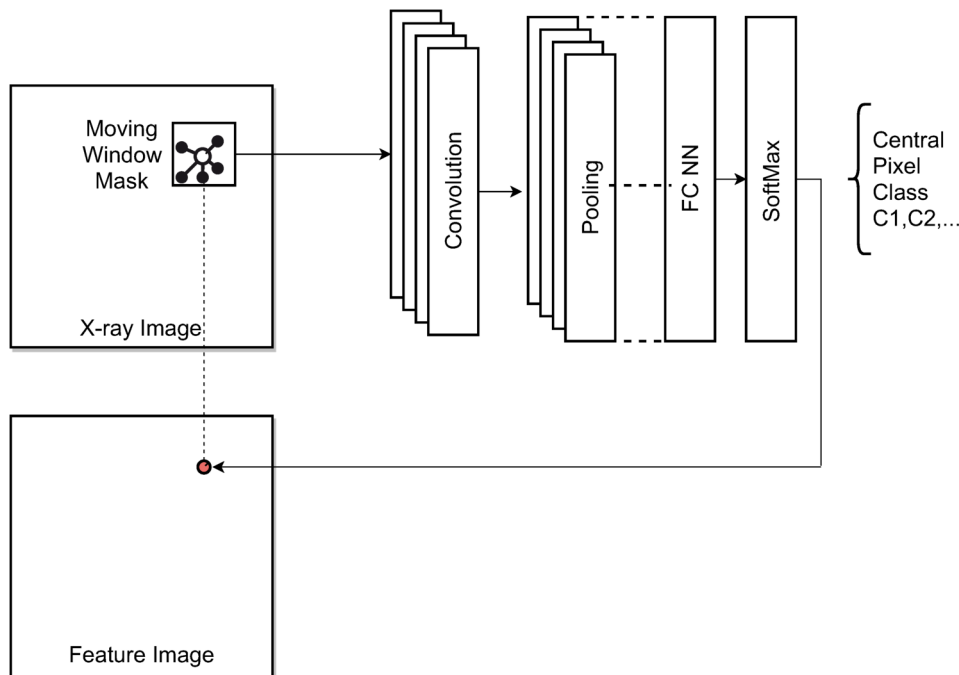

Fig. 8. Semantic pixel classifier applied to X-ray single projection images to detect and mark hidden defects

The pixel classifier is trained supervised with labelled regions of pores (i.e., pixels inside a closed polygon path surrounding a pore in the image), as discussed in the following Sec. 5.

5. Experiments

Experiments were carried out with aluminum die casted plates (150 mm × 40 mm × 3 mm) containing process gas pores. The objective is to find a simple pore feature marking pixel detector that maps a X-ray single projection image on a feature image marking all pores. The aluminum die casted plates as well as the MidQ reference measurements were contributed by Dirk Lehmhus, Fraunhofer IFAM, Bremen, Germany.

In addition to the feature detection experiments, the low-cost and low-quality X-ray measuring device is compared with the aforementioned commercial device with respect to noise, spatial resolution, contrast, and geometric distortions.

In Figures 9 and 10 single projection X-ray images and a profile analysis are shown, measured with the reference Mid Q and the LowQ devices. Only a few big pores can be easily detected by visual inspection. The contrast of the biggest pore peak is C(MidQ) = 1.42 and C(LowQ) = 1.86. The FWHM of the pore peak is FWHM(MidQ) = 7px ≈ 0.7 mm and FWHM(LowQ) = 25px ≈ 0.75 mm.
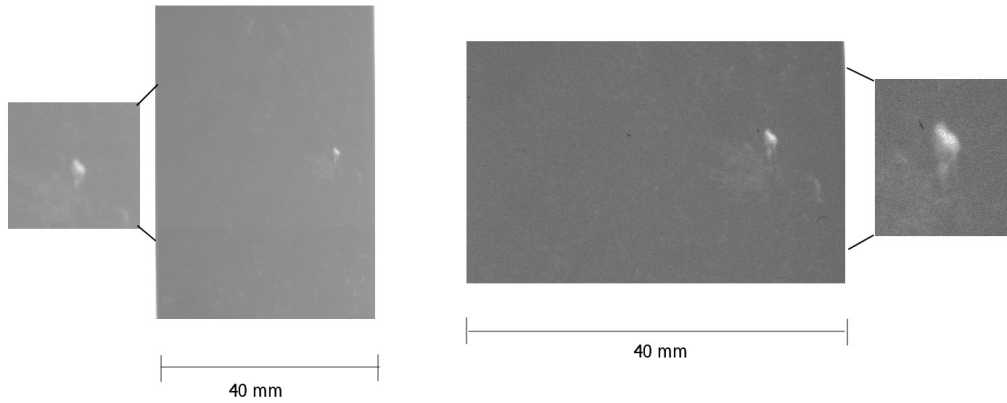
Fig. 9. X-ray image sections from MidQ (left) and LowQ (right) device, respectively, of a selected hidden pore in a aluminum high-pressure die casted plate (Pixel scaling: Left 100μm/pixel, Right: 30μm/pixel)
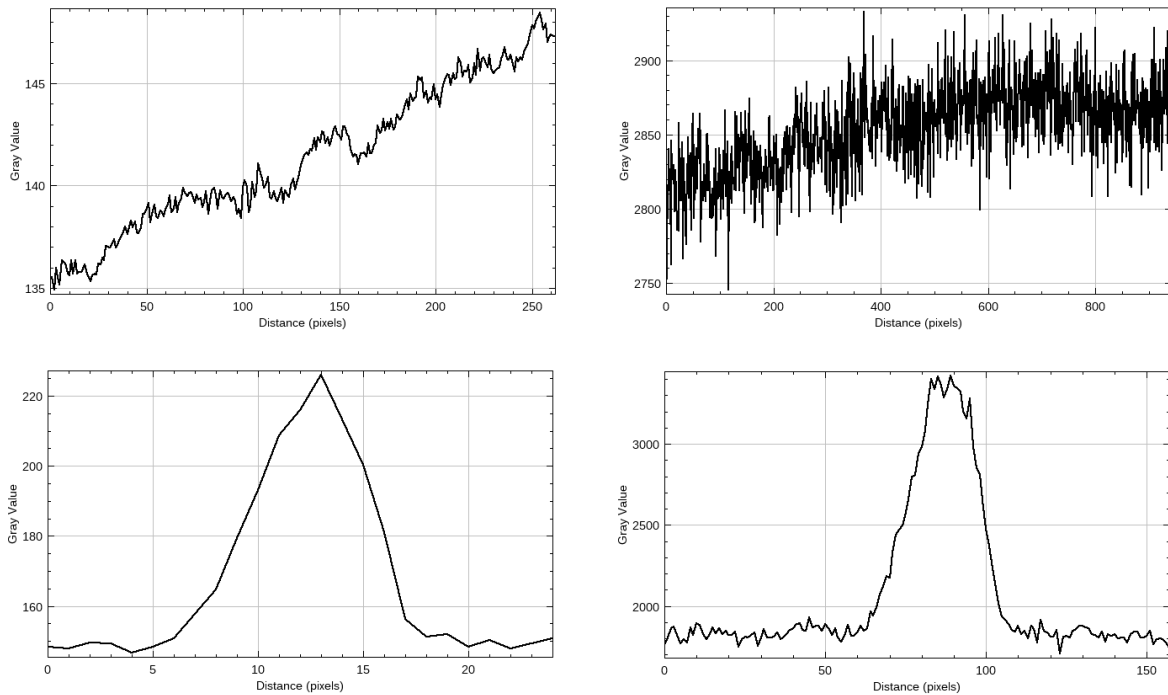

Fig. 10. Comparison of MidQ (left) and LowQ (right) measurement results from an aluminum die casted plate with pores (Top) Averaged slice intensity of mostly homogeneous area (Bottom) Averaged slice intensity (average over vertically 20/3 pixels) of a strong pore. M_{xray}=2.0(MidQ)/1.0(LowQ), $s_{px,eff}$=100μm(MidQ)/30μm(LowQ), exposure time t=100ms (MidQ) / 2×5s (LowQ)

The main objective of this work is the application of the semantic pixel classifier for feature marking of pores in aluminum die casted plates using single projection sampled with the LowQ device introduced in this paper. Since there is no ground truth in the measured images, i.e., accurate labelling for training is not possible, synthetic images retrieved from numerical X-ray simulation were used for the training of the pixel classifier, finally applied to X-ray images.
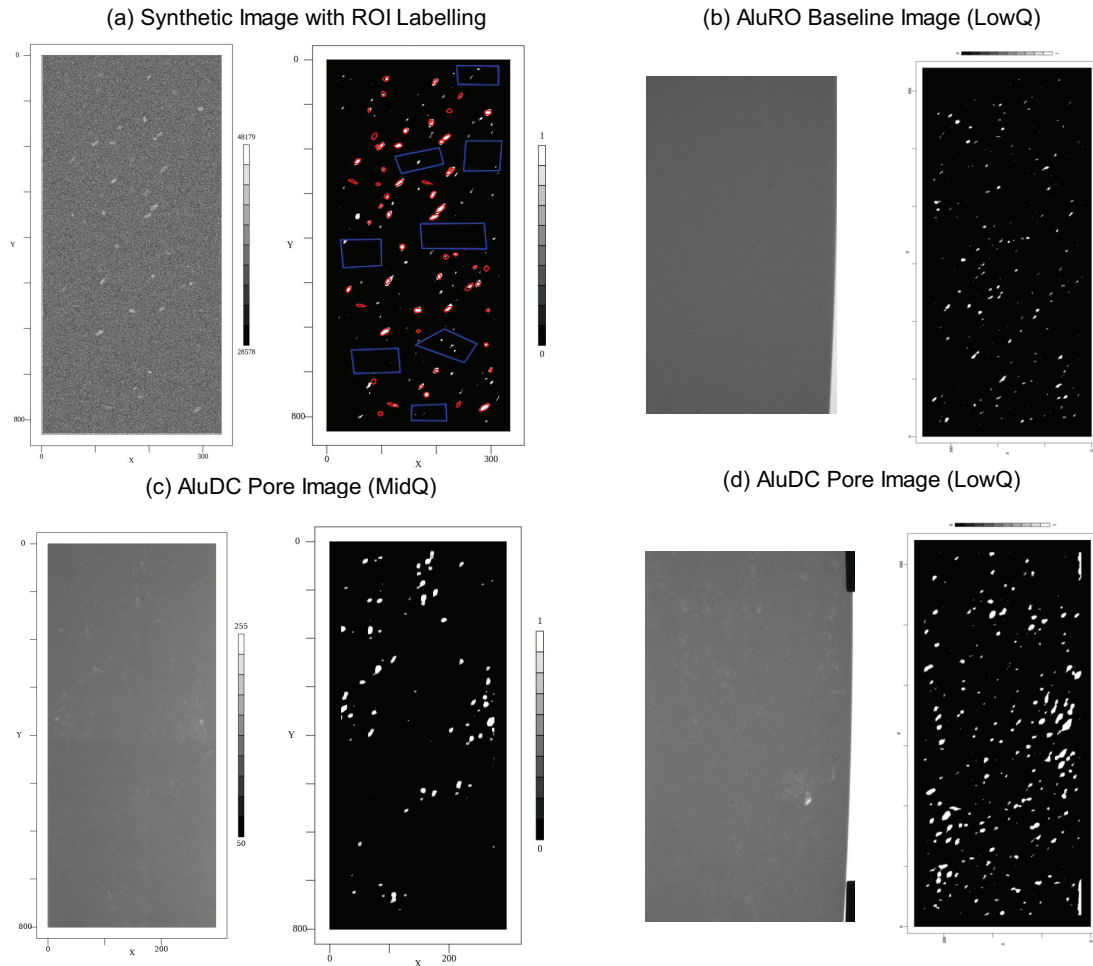

Fig. 11. Results of the feature marking for different X-ray images using a selected sample plate and two measuring instruments and synthetic images. Note that the LowQ images have a different scaling and region compared to the MidQ and synthetic X-ray images. aluDC: Die casted aluminum plate with pores, aluRO: Rolled and polished aluminum plate without pores.

Fig. 11 shows some selected results. There are always image pairs shown consisting of the X-ray input image (left) and the pore feature marking image (right) as predicted by the semantic pixel classifier. One of the synthetic images and the prediction of the trained model is shown in Fig. 11 (a). Additionally, the feature image shows the ROI selection and labelling of the input images used for training (red: pore area, blue: selected background regions). The ROIs were automatically created from the CAD model used for simulation.

The predictor model was trained with 40 epochs. The CNN architecture consists of two convolution-pooling layer pairs with 8 filters each. The training set consisted of an imbalanced set preferring background examples to suppress false positive predictions rather than false negative. Since there is no ground truth for the measured images, we can evaluate only the results for the synthetic images. The overall accuracy achieved on a test set is 93%, with a class-specific error of 4% background and 11% pore region marking. The F1 score is 0.93. These results sound promising, and examples of feature marking of measured images is shown in Fig. 11 (c) and (d) for the low-noise MidQ and noisy LowQ instruments, respectively. It can be seen that there is a significantly increased pore feature marking in the LowQ images compared with the MidQ images. To estimate the impact of noise (from detector and radiation source) we tested a pore-free rolled and polished aluminum plate, as shown in Fig. 11 (b), applying the same predictor model and expecting a black image, but it is not. This shows clearly the noise sensitivity of the predictor model, which must be suppressed. An approach to discriminate noise from pores in the feature marking images is to calculate the union of two independent images from the same specimen, as it is expected (and can be shown) that noisy marking are randomly positioned. Geometric distortions of the LowQ system seems to be irrelevant for the feature marking process.

6. Conclusions

One of the main findings of this work is that a low-cost constraint does not result necessarily in low-quality output (although, LowQ device named in this work). With respect to resolution and contrast the LowQ device outperforms an industrial MidQ device, but noise is significantly higher due to lower overall sensitivity and long exposure times not allowing extra exposure required to reduce image noise significantly. Additionally, random popcorn/shot noise in the LowQ indirect imaging system requires at least two independent images to remove this noise substantially.

The higher noise of the LowQ instrument compared with the industrial MidQ device has a significant impact on the accuracy and quality of the data-driven feature marking model. Geometric distortions of the LowQ system seems to be irrelevant for the feature marking process. It was possible to train the feature marking detector with pure synthetic X-ray images computed by a numerical simulator using a CAD model of the specimen with randomly created defects.

Future work must improve the training data set by overlaying measured noise (especially from the LowQ device) to the simulated X-ray images.

7. Acknowledgments

8. References

[1]   B. Hena, Z. Wei, C. I. Castanedo, and X. Maldague, *Deep Learning Neural Network Performance on NDT Digital X-ray Radiography Images: Analyzing the Impact of Image Quality Parameters—An Experimental Study*, sensors, vol. 23, no. 4324, 2023

[2]   R. Booto Tokime, X. Maldague, *Automatic Defect Detection for X-Ray inspection: Identifying defects with deep convolutional network*, Canadian Institute for Non-destructive Evaluation (CINDE) 2019, Edmonton, Canad, (2019)

[3]   gvirtualxray, https://gvirtualxray.fpvidal.net, accessed on-line on 24.1.2023

[4]   F. P. Vidal, *Introduction to X-ray simulation on GPU using gVirtualXRay*, In Workshop on Image-Based Simulation for Industry 2021 (IBSim-4i 2020), London, UK, October, 2021

[5]   S. L. Balasubramanian and G. Krishnamurthi, *X-ray scintillator lens-coupled with CMOS camera for pre-clinical cardiac vascular imaging—A feasibility study*, PLOS One, vol. 17, no. 2, 2022.

[6]   Carl Zeiss, *Resolution of a 3D X-ray Microscope - Defining Meaningful Resolution Parameters for XRM*, technical note, Carl Zeiss Microscopy GmbH, Germany, July 2013

[7]   CAWO, *Green-emitting Screens*, https://www.cawo.com/products/intensifying-screens/green-emitting, accessed on-line 13.9.2023

[8]   FRAMOS, *FSM-IMX290 Datasheet*, https://www.framos.com